 CMES, vol.114, no.2, pp.239-259, 2018

Micromechanics-Based Elastic Fields of Closed-Cell Porous Media

Lianhua Ma[1] and Qingsheng Yang[2, *]

Abstract: Fluid-filled closed-cell porous media could exhibit distinctive features which are influenced by initial fluid pressures inside the cavities. Based on the equivalent far-field method, micromechanics-based solutions for the local elastic fields of porous media saturated with pressurized fluid are formulated in this paper. In the present micromechanics model, three configurations are introduced to characterize the different state the closed-cell porous media. The fluid-filled cavity is assumed to be a compressible elastic solid with a zero shear modulus, and the pressures in closed pores are represented by eigenstrains introduced in fluid domains. With the assumption of spheroidal fluid-filled pores, the local stress and strain fields in solid matrix of porous media are derived by using the Exterior-Point Eshelby tensors, which are dependent of the Poisson's ratio of solid matrix and the locations of the investigated material points outside the spheroidal fluid domain. The reliability and accuracy of the analytical elastic solutions are verified by a classical example. Moreover, for finite volume fraction of the fluid inclusions, the local elastic fields of the porous media subjected to the initial fluid pressure and external load are obtained. The results show that the present micromechanics model provides an effective approach to characterize the local elastic fields of the materials with closed-cell fluid-filled pores.

Keywords: Porous media, fluid-filled pores, local elastic fields, fluid pressure, micromechanics.

1 Introduction

In classical micromechanics of composites, the emphasis was focused on mechanical properties of composites with solid inclusions in previous investigations. Meanwhile, the macroscopic properties of porous media with the fluid inclusions and the internal pressures in the closed cavities have already been paid more and more attention. Closed-cell porous medium containing the fluid phase with or without internal pressure is a special kind of composite, which is widely applied in practical engineering. The mechanical behaviors of the porous media are affected by the initial fluid pressure in the cavity.

[1] College of Civil Engineering and Architecture, Hebei University, Baoding, 071002, China

[2] Department of Engineering Mechanics, Beijing University of Technology, Beijing 100124, China.

* Corresponding author: Qingsheng Yang. Email: qsyang@bjut.edu.cn.

For a porous material, the micro-scale pores and interstitial fluid have an important effect on the macroscopic properties of the material. Several researchers have studied the effective mechanical properties of the materials. The poroelastic mechanics models of saturated porous medium have been founded, see Terzaghi [Terzaghi (1943)], Gassmann [Gassmann (1951)], Biot [Biot (1954)]. Hereafter, O'Connell and Budiansky [O'Connell and Budiansky (1977)] analyzed the influences of local fluid flow on the poroelasticity of the materils containing arbitrary holes. Thomsen [Thomsen (1995)] applied the anisotropic elastic theory to the porous media. In addition, Ozgur et al. [Ozgur, Mullen and Welsch (1996)], Kachanov et al. [Kachanov, Tsukrov and Shafiro (1995)] and Shafiro et al. [Shafiro and Kachanov (1997)] studied the effects of the hydrostatic fluid on macroscopic mechanical properties of closed-cell materials and the phenomenon of the pressure polarization. Hartmann et al. [Hartmann and Delgado (2004); Hartmann, Mathmann and Delgado (2006)] simulated the compressive deformation of yeast cells under high hydrostatic pressure. Yang and Li [Yang and Li (2006)] established a micromechanical model to study the microstructure and effective property evolution of the cement hydration process. Ma et. al [Ma, Rolfe, Yang et al. (2011); Ma, Yang, Yan et al. (2014)] developed a micromechanics model to investigate the effects of the fluid pressure and gas pressure on the macroscopic mechanical properties of the close-cell porous materials. In recent years, the numerical techniques, for example, multi-scale finite element method [Zhang, Lv and Zheng (2010)], boundary element method [Huang, Zheng and Yao (2011)] and computational homogenization approach [Ma, Rolfe, Yang et al. (2011); Ma, Yang, Yan et al. (2014)] have been proposed to solve the elastic fields of porous media with closed fluid. Guo et al. [Guo and Cheng (2002)] modified the classical Gurson model [Gurson (1977)] of porous material by introducing the effect of the gas pressure. Chen et al. [Chen, Zhu, Wang et al. (2006)], Kitazono et al. [Kitazono, Sato and Kuribayashi (2003)] and Zhang et al. [Zhang, Xu, Wang el al. (2009)] developed micromechanical models to study the macro-elastoplastic properties of the closed-cell porous materials. Vincent et al. [Vincent, Monerie and Suquet (2009)] adopted Gurson-like approach [Gologanu, Leblond and Devaux (1994)] and variational method [Ponte Castañeda (1991)] to derive the upper bounds of macroscopic plastic properties of closed-cell porous media with different internal pressures, and an N-phase model was proposed which matches the best of the bounds. Further, Julien et al. [Julien, Garajeu and Michel (2011)] used the N-phase micromechanical model to study the macroscopic plastic behavior of porous materials with viscoplastic matrix. These studies have revealed the significance of a fluid inclusion phase on the macroscopic mechanical properties of closed-cell porous media.

The micromechanics models have been widely developed based on Eshelby equivalent inclusion principle [Eshelby (1957)] to study the macroscopic properties of composites. However, for the composites with the finite volume fraction of inclusions, the problem of the local elastic fields of the matrix is an important issue which has drawn wide attention. Eshelby [Eshelby (1957)] and Mura [Mura (1987)] found the solution of exterior elastic field of a spheroidal inclusion in the infinite matrix. However, the expressions were given in terms of complicated elliptic integrals. The displacement potential function method can be used to solve the local elastic fields outside the spheroidal inclusion. Mikata et al. [Mikata and Taya (1985)] analyzed a stress field for the spheroidal inclusions under

axisymmetric loadings. Ju et al. [Ju and Sun (1999)] introduced a virtual spheroidal inclusion inside the matrix to calculate the local elastic field of the infinite matrix. Duan et al. [Duan, Wang, Huang et al. (2005)] obtained the elastic solution of the infinite matrix under far-field axisymmetric loadings for the arbitrary orientation of the spheroidal inclusions with interphase. Guo et al. [Guo, Liu and Hu (2006)] applied the maximum information entropy theory and the secant modulus method to study the local stress field of the composites. Most contributions in the literatures are concerned with the determination of elastic fields of conventional composite and porous material. The local elastic solutions of closed-cell porous media saturated with pressurized fluid are seldom reported. In this paper, a micromechanical model based on an equivalent far-field approach is presented to formulate the local elastic fields of closed-cell porous media filled with pressurized fluids.

2 Equivalent far-field method

To reveal the local elastic fields of closed-cell porous media containing the fluid and internal pressure, the notion of the representative volume element (RVE) and the equivalent far-field method are used to transform the problem of finite volume fraction into the one of infinite matrix. We first consider the material containing closed fluid inclusions without initial fluid pressure. Because the closed fluid cannot have the shear and tensile resistance, its shear modulus is zero, i.e. $\mu_f = 0$. Considering the compressibility of the fluid-filled cavity, the compression stiffness tensor of the closed fluid can be expressed as $C^f_{ijkl} = k_f \delta_{ij} \delta_{kl}$, where k_f is the bulk modulus of the fluid inclusion, δ_{ij} is the Kronecker delta. For the material with multiple spheroidal inclusions, it is assumed that the closed fluid does not penetrate each other. For convenience, the material containing a cluster of fluid-filled inclusions is selected and the boundary condition of uniform traction $\mathbf{t}^0 = \boldsymbol{\sigma}^0 \cdot \mathbf{n}$ is applied, where $\mathbf{n}$ is the external normal of the body's surface, $\boldsymbol{\sigma}^0$ is the uniform stress. The average stress over the heterogeneous material can be obtained [Mura (1987); Yang and Becker (2004); Yang, Tao and Yang (2007)].

$$\bar{\boldsymbol{\sigma}} = \boldsymbol{\sigma}^0 \tag{1}$$

Then the macroscopic constitutive relation of the material can be expressed by

$$\boldsymbol{\sigma}^0 = \bar{\mathbf{C}} : \bar{\boldsymbol{\varepsilon}} \tag{2}$$

where $\bar{\mathbf{C}}$ is the unknown effective elastic stiffness, $\bar{\boldsymbol{\varepsilon}}$ is the average strain over the material.

In order to apply the Eshelby equivalent inclusion theory [Eshelby (1957)] to the present problem of finite volume fraction inclusions, the RVE is put into the infinite matrix subjected to the far-field stress $\boldsymbol{\sigma}^\infty$. The elastic field generated by far-field stress $\boldsymbol{\sigma}^\infty$ should be consistent with that caused by uniform stress $\boldsymbol{\sigma}^0$. In other words, it is

equivalent for $\boldsymbol{\sigma}^0$ applied in boundaries and $\boldsymbol{\sigma}^\infty$ applied in the far field, as shown in Fig. 1. This is the main idea of the equivalent far-field method.

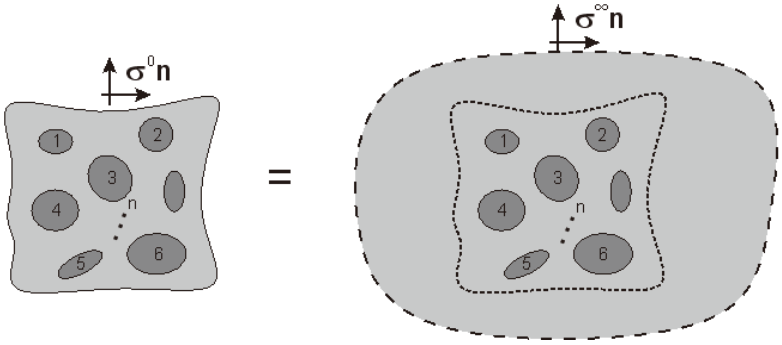

Figure 1: Equivalent far-field model of the RVE subjected to uniform stress boundary condition

3 Equivalent micromechanical model

For discussion of the local elastic fields of the RVE of closed-cell porous media containing fluid and internal pressure, three configurations, i.e., reference configuration, natural configuration and current configuration, can be defined here. The reference configuration is referred to as the state of free stress in the matrix and fluid phase. If an initial pressure is imposed on the fluid domain in reference configuration, the RVE experiences an initial elastic fields in matrix. This equilibrium state is called natural configuration where the initial fluid pressure is characterized by p_0. When an external traction is successively imposed on the boundary of RVE, the current configuration can be achieved, and the fluid pressure is changed to p, due to the compressibility of the fluid. This means that the current configuration of the RVE is produced by the initial fluid pressure and external uniform stress simultaneously. Accordingly, the total local elastic fields of current configuration can be obtained by summing local elastic fields by the initial fluid pressure and by the external force. Fig. 2 depicts the evolution of the three configurations of the RVE.

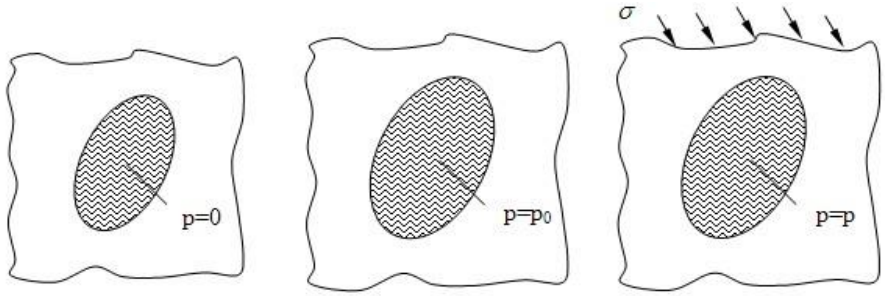

(a) reference configuration (b) natural configuration (c) current configuration

Figure 2: Evolution of three configurations of the RVE

For the single fluid inclusion material with the volume fraction f_1 of the inclusions, the local elastic fields caused by the initial fluid pressure in the natural configuration are analyzed. In this case, the initial elastic fields in the natural configuration of the RVE are entirely caused by the initial fluid pressure.

In order to obtain the initial elastic fields of the RVE containing the finite volume fraction of closed fluid and initial internal pressure, by using the equivalent far-field method, the material in reference configuration is put into infinite matrix subjected to the far-field stress $\boldsymbol{\sigma}^{\infty}$, and an initial eigenstrain $\boldsymbol{\varepsilon}^{p_0}$ is applied to the fluid-filled pore , which can represent the initial fluid pressure p_0. If the local elastic fields produced by the equivalent far-field model within the RVE are consistent with the local elastic fields produced in natural configuration, the local fields problem of initial model is completely equivalent to the far-field model, as shown in Fig. 3.

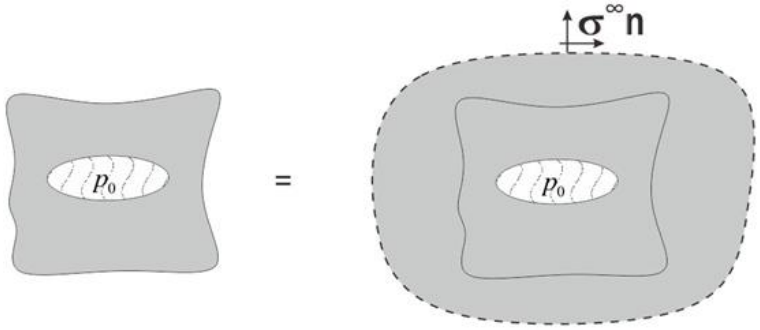

Figure 3: Equivalent far-field model of the RVE in natural configuration

The equivalent inclusion method [Eshelby (1957)] is usually used to evaluate residual stresses of a composite [Takao and Taya (1985); Hu and Weng (1998)]. Utilizing this method, the initial stress $\mathbf{P}^0$ of fluid inclusions can be expressed as,

$$\mathbf{P}^0 = -p_0\mathbf{I} = \mathbf{C}_1 : \left(\boldsymbol{\varepsilon}^{\infty} + \tilde{\boldsymbol{\varepsilon}}_1 - \boldsymbol{\varepsilon}^{p_0}\right) = \mathbf{C}_0 : \left(\boldsymbol{\varepsilon}^{\infty} + \tilde{\boldsymbol{\varepsilon}}_1 - \boldsymbol{\varepsilon}^{*} - \boldsymbol{\varepsilon}^{p_0}\right) \tag{3}$$

where $\mathbf{I}$ is the second-order unit tensor. $\mathbf{C}_0$ and $\mathbf{C}_1$ are the elastic stiffness for matrix and inclusions respectively. $\boldsymbol{\varepsilon}^{\infty}$ is the equivalent far-field strain, $\tilde{\boldsymbol{\varepsilon}}_1$ is the perturbing strain of the fluid inclusions, $\boldsymbol{\varepsilon}^{*}$ is the eigenstrain of the fluid inclusions because $\mathbf{C}_1$ is replaced by $\mathbf{C}_0$ in Eq. (3). By using the self-equilibrium condition, the relationship between the equivalent far-field strain $\boldsymbol{\varepsilon}^{\infty}$ and the initial fluid pressure p_0 can be given by

$$\boldsymbol{\varepsilon}^{\infty} = -\frac{f_1}{1-f_1}\mathbf{C}_0^{-1} : \mathbf{P}^0 \tag{4}$$

Consequently, the equivalent far-field stress is

$$\boldsymbol{\sigma}^{\infty} = \mathbf{C}_0 : \boldsymbol{\varepsilon}^{\infty} = -\frac{f_1}{1-f_1}\mathbf{P}^0 \tag{5}$$

By the equivalent inclusions principle, the strain of fluid inclusion $\boldsymbol{\varepsilon}^{\infty}+\tilde{\boldsymbol{\varepsilon}}_1$ and the eigenstrain $\boldsymbol{\varepsilon}^{*}$ can be easily derived as

$$\boldsymbol{\varepsilon}^{\infty}+\tilde{\boldsymbol{\varepsilon}}_1=\mathbf{A}:\boldsymbol{\varepsilon}^{\infty}+\mathbf{a}:\boldsymbol{\varepsilon}^{p_0} \tag{6}$$

$$\boldsymbol{\varepsilon}^{*}=\left(\mathbf{S}+\left(\mathbf{C}_1-\mathbf{C}_0\right)^{-1}:\mathbf{C}_0\right)^{-1}\left[\left(\mathbf{I}'-\mathbf{S}\right):\boldsymbol{\varepsilon}^{p_0}-\boldsymbol{\varepsilon}^{\infty}\right] \tag{7}$$

where $\mathbf{I}'$ is the fourth-order unit tensor, $\mathbf{S}$ is the fourth-order Eshelby's tensor depending on the shape of the inclusion and elastic properties of the solid matrix, and

$$\mathbf{A}=\left[\mathbf{I}'+\mathbf{S}:\mathbf{C}_0^{-1}:\left(\mathbf{C}_1-\mathbf{C}_0\right)\right]^{-1} \tag{8}$$

$$\mathbf{a}=-\left(\mathbf{C}_0-\mathbf{C}_0:\mathbf{S}^{-1}-\mathbf{C}_1\right)^{-1}:\mathbf{C}_1 \tag{9}$$

From Eq. (3), we can obtain

$$\boldsymbol{\varepsilon}^{\infty}+\tilde{\boldsymbol{\varepsilon}}_1-\boldsymbol{\varepsilon}^{*}-\boldsymbol{\varepsilon}^{p_0}=\mathbf{C}_0^{-1}:\mathbf{P}^0 \tag{10}$$

By combining Eqs. (6), (7) and (10), the strain $\boldsymbol{\varepsilon}^{p_0}$ is then obtained as

$$\boldsymbol{\varepsilon}^{p_0}=\left(\mathbf{a}-\mathbf{I}'-\left(\mathbf{S}+\mathbf{M}\right)^{-1}:\left(\mathbf{I}'-\mathbf{S}\right)\right)^{-1}\left(\mathbf{C}_0^{-1}:\mathbf{P}^0-\mathbf{A}:\boldsymbol{\varepsilon}^{\infty}-\left(\mathbf{S}+\mathbf{M}\right)^{-1}:\boldsymbol{\varepsilon}^{\infty}\right) \tag{11}$$

Substitution of Eq. (4) into Eq. (11) yields

$$\boldsymbol{\varepsilon}^{p_0}=\left(\mathbf{a}-\mathbf{I}'-\left(\mathbf{S}+\mathbf{M}\right)^{-1}:\left(\mathbf{I}'-\mathbf{S}\right)\right)^{-1}\left(\mathbf{C}_0^{-1}:\mathbf{P}^0+\frac{f_1}{1-f_1}\mathbf{A}:\mathbf{C}_0^{-1}:\mathbf{P}^0+\frac{f_1}{1-f_1}\left(\mathbf{S}+\mathbf{M}\right)^{-1}:\mathbf{C}_0^{-1}:\mathbf{P}^0\right) \tag{12}$$

As seen in Eqs. (5) and (12), it is obvious that for the RVE containing initial fluid pressure in the natural configuration, the far-field stress $\boldsymbol{\sigma}^{\infty}$ in the equivalent far-field model and the applied initial eigenstrain $\boldsymbol{\varepsilon}^{p_0}$ can be expressed as a function in terms of the given initial fluid pressure p_0.

In the current configuration, total elastic fields of the RVE can be divided into the individual effect of the initial fluid pressure and the external uniform stress, while the relationship between the equivalent far-field stress and the initial fluid pressure is demonstrated by Eqs. (5) and (12). Therefore, we only consider the case of material subjected to external uniform stress in order to obtain the local elastic fields. In the current configuration, the boundary condition of uniform stress of the RVE is $\mathbf{t}^0=\boldsymbol{\sigma}^0\cdot\mathbf{n}$. For the transformed far-field model, the RVE is subjected to the boundary condition of far-field uniform traction $\mathbf{t}^{\infty}=\overline{\boldsymbol{\sigma}}^{\infty}\cdot\mathbf{n}$. Based on the equivalent far-field method, the elastic fields produced by uniform stress $\overline{\boldsymbol{\sigma}}^{\infty}$ of the far-field boundary are consistent with the elastic fields produced by uniform stress $\boldsymbol{\sigma}^0$ on the boundary. Thus, these models can be considered to be equivalent completely, as shown in Fig. 4.

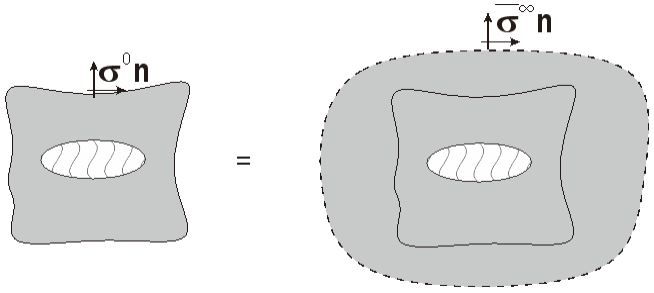

Figure 4: Equivalent far-field model in the current configuration

On the basis of the principle of the equivalent inclusions, the internal stress generated in fluid domain can be expressed by

$$\mathbf{C}_1 : \left(\overline{\boldsymbol{\varepsilon}}^{\infty} + \tilde{\boldsymbol{\varepsilon}}\right) = \mathbf{C}_0 : \left(\overline{\boldsymbol{\varepsilon}}^{\infty} + \tilde{\boldsymbol{\varepsilon}} - \overline{\boldsymbol{\varepsilon}}^{*}\right) \tag{13}$$

where $\overline{\boldsymbol{\varepsilon}}^{\infty}$ is the uniform strain corresponding to the uniform far-field stress $\overline{\boldsymbol{\sigma}}^{\infty}$, i.e. $\overline{\boldsymbol{\sigma}}^{\infty} = \mathbf{C}_0 : \overline{\boldsymbol{\varepsilon}}^{\infty}$. $\tilde{\boldsymbol{\varepsilon}}$ is the perturbing strain in the fluid inclusion. $\overline{\boldsymbol{\varepsilon}}^{*}$ is the equivalent eigenstrain as the fluid inclusion is replaced by the matrix material. The perturbing strain $\tilde{\boldsymbol{\varepsilon}}$ and $\overline{\boldsymbol{\varepsilon}}^{*}$ of the fluid inclusions have the following relation [Eshelby (1957)]

$$\tilde{\boldsymbol{\varepsilon}} = \mathbf{S} : \overline{\boldsymbol{\varepsilon}}^{*} \tag{14}$$

Then we can get the total strain of fluid inclusions

$$\overline{\boldsymbol{\varepsilon}}^{\infty} + \tilde{\boldsymbol{\varepsilon}} = \mathbf{A} : \overline{\boldsymbol{\varepsilon}}^{\infty} \tag{15}$$

Using the equivalent far-field method, we can establish the relationship between the uniform stress $\boldsymbol{\sigma}^0$ and the uniform equivalent far-field strain $\overline{\boldsymbol{\varepsilon}}^{\infty}$

$$\boldsymbol{\sigma}^0 = \left(f_0\mathbf{C}_0 + f_1\mathbf{C}_1 : \mathbf{A}\right) : \overline{\boldsymbol{\varepsilon}}^{\infty} \tag{16}$$

The uniform strain $\overline{\boldsymbol{\varepsilon}}^{\infty}$ of equivalent far-field can be written as

$$\overline{\boldsymbol{\varepsilon}}^{\infty} = \mathbf{C}_0^{-1} : \overline{\boldsymbol{\sigma}}^{\infty} \tag{17}$$

Combining Eqs. (16) and (17), we can get the relationship between the uniform equivalent far-field stress $\overline{\boldsymbol{\sigma}}^{\infty}$ and the boundary uniform stress $\boldsymbol{\sigma}^0$.

$$\overline{\boldsymbol{\sigma}}^{\infty} = \mathbf{C}_0 : \left(f_0\mathbf{C}_0 + f_1\mathbf{C}_1 : \mathbf{A}\right)^{-1} : \boldsymbol{\sigma}^0 \tag{18}$$

This formula shows that under the finite volume fraction, for the given boundary uniform stress $\boldsymbol{\sigma}^0$, the far-field stress $\boldsymbol{\sigma}^{\infty}$ in the equivalent far-field model can be expressed in terms of $\boldsymbol{\sigma}^0$.

Utilizing the principle of superposition, the total equivalent far-field stress $\boldsymbol{\sigma}_t^{\infty}$ of the RVE in the current configuration can be expressed as the sum of the equivalent far-field stresses caused by the initial fluid pressure p_0 and external uniform stress $\boldsymbol{\sigma}^0$. That is

$$\boldsymbol{\sigma}_t^{\infty} = \boldsymbol{\sigma}^{\infty} + \overline{\boldsymbol{\sigma}}^{\infty} = -\frac{f_1}{1-f_1}\mathbf{P}^0 + \mathbf{C}_0 : \left(f_0\mathbf{C}_0 + f_1\mathbf{C}_1 : \mathbf{A} \right)^{-1} : \boldsymbol{\sigma}^0 \tag{19}$$

By means of the above derivation, we can respectively obtain the equivalent far-field stress in the natural and current configuration of the investigated material with the initial fluid pressure. As a result, the problem of finite volume fraction is translated into the problem of infinite matrix through the equivalent far-field method.

4 Local elastic fields

For a spheroidal inclusion embedded into the infinite matrix D, as the whole material is subjected to a boundary condition of uniform stress in far-field and a uniform eigenstrain in the inclusion domain Ω, the Eshelby tensor **S** is independent of the local coordinates. Moreover, the strain and stress in inclusion are uniform for this case. The details can be found in literature [Mura (1987)].

According to the equivalent far-field model and Eshelby solution of infinite matrix, the elastic fields in fluid domains can be obtained in current configuration

$$\boldsymbol{\varepsilon} = \boldsymbol{\varepsilon}_t^{\infty} + \mathbf{S} : \boldsymbol{\varepsilon}^{**} \qquad (\text{in } \Omega) \tag{20}$$

$$\boldsymbol{\sigma} = \boldsymbol{\sigma}_t^{\infty} + \mathbf{C}_0 : (\mathbf{S} - \mathbf{I}') : \boldsymbol{\varepsilon}^{**} \quad (\text{in } \Omega) \tag{21}$$

where $\boldsymbol{\varepsilon}_t^{\infty}$ is the equivalent far-field strain corresponding to the equivalent far-field stress $\boldsymbol{\sigma}_t^{\infty}$ in the current configuration. According to $\boldsymbol{\sigma}_t^{\infty} = \mathbf{C}_0 : \boldsymbol{\varepsilon}_t^{\infty}$ and Eq. (19), the equivalent far-field strain can be given by

$$\boldsymbol{\varepsilon}_t^{\infty} = -\frac{f_1}{1-f_1}\mathbf{C}_0^{-1} : \mathbf{P}^0 + \left(f_0\mathbf{C}_0 + f_1\mathbf{C}_1 : \mathbf{A} \right)^{-1} : \boldsymbol{\sigma}^0 \tag{22}$$

In addition, the total eigenstrain $\boldsymbol{\varepsilon}^{**}$ is the sum of the eigenstrain $\boldsymbol{\varepsilon}^{p_0}$ produced by the initial fluid pressure p_0 and the equivalent eigenstrain in inclusions caused by equivalent far-field traction

$$\boldsymbol{\varepsilon}^{**} = \left(\mathbf{S} + \mathbf{M} \right)^{-1} : \left(\mathbf{N} : \boldsymbol{\varepsilon}^{p_0} - \boldsymbol{\varepsilon}_t^{\infty} \right) \tag{23}$$

where **M** and **N** are the fourth-order tensors, respectively

$$\mathbf{M} = \left(\mathbf{C}_1 - \mathbf{C}_0 \right)^{-1} : \mathbf{C}_0 \tag{24}$$

$$\mathbf{N} = \left(\mathbf{C}_1 - \mathbf{C}_0 \right)^{-1} : \mathbf{C}_1 \tag{25}$$

The local elastic fields of matrix outside the inclusions are no longer uniform. In order to obtain the external local elastic fields, a fourth-order tensor $\bar{\mathbf{G}}(\mathbf{x})$, called Exterior-Point Eshelby tensor, is introduced to describe the local elastic field of the solid matrix

$$\bar{\mathbf{G}}(\mathbf{x}) = \int_{\Omega} \mathbf{G}(\mathbf{x} - \mathbf{x}') \mathrm{d}\mathbf{x}', \quad (\text{in D} - \Omega) \tag{26}$$

where $\mathbf{G}(\mathbf{x}-\mathbf{x}')$ is the Green function, $\mathbf{x}$ is a material point of matrix domain $\mathrm{D}-\Omega$ outside the inclusions. The Green function can be written by

$$\begin{aligned} G_{ijkl}(\mathbf{x}-\mathbf{x}') = & \frac{1}{8\pi(1-\nu_0)\|\mathbf{x}-\mathbf{x}'\|^3}(1-2\nu_0)\left(\delta_{ik}\delta_{jl}+\delta_{il}\delta_{jk}-\delta_{ij}\delta_{kl}\right) \\ & +3\nu_0\left(\delta_{ik}n_jn_l+\delta_{il}n_jn_k+\delta_{jk}n_in_l+\delta_{jl}n_in_k\right)+3\delta_{ij}n_kn_l+3(1-2\nu_0)\delta_{kl}n_in_j-15n_in_jn_kn_l \end{aligned} \tag{27}$$

where ν_0 is the Poisson's ratio of matrix material, $\mathbf{n}$ is the unit vector of outward normal defined by $\mathbf{n}=(\mathbf{x}-\mathbf{x}')/\|\mathbf{x}-\mathbf{x}'\|$. Once we get the Exterior-Point Eshelby tensor $\bar{\mathbf{G}}(\mathbf{x})$, the local elastic fields of the solid matrix outside fluid inclusions in the current configuration can be expressed by

$$\boldsymbol{\varepsilon}(\mathbf{x})=\boldsymbol{\varepsilon}_t^{\infty}+\bar{\mathbf{G}}(\mathbf{x}):\boldsymbol{\varepsilon}^{**} \quad (\text{in } \mathrm{D}-\Omega) \tag{28}$$

$$\boldsymbol{\sigma}(\mathbf{x})=\boldsymbol{\sigma}_t^{\infty}+\mathbf{C}_0:\bar{\mathbf{G}}(\mathbf{x}):\boldsymbol{\varepsilon}^{**} \quad (\text{in } \mathrm{D}-\Omega) \tag{29}$$

As can be seen from Eqs. (28) and (29), the Exterior-Point Eshelby tensor $\bar{\mathbf{G}}(\mathbf{x})$ is similar to the Eshelby tensor $\mathbf{S}$ for the local field inside the fluid inclusion of the porous media. As the expression of $\bar{\mathbf{G}}(\mathbf{x})$ is derived, the local elastic fields outside the inclusion can be determined exactly. The explicit expressions of the Exterior-Point Eshelby tensor $\bar{\mathbf{G}}(\mathbf{x})$ of spheroidal inclusions were given by Ju et al. [Ju and Sun (1999)].

The local elastic fields in matrix induced only by initial fluid pressure can be obtained as

$$\boldsymbol{\varepsilon}(\mathbf{x})=\boldsymbol{\varepsilon}_0^{\infty}+\bar{\mathbf{G}}(\mathbf{x}):\boldsymbol{\varepsilon}_0^{**} \quad (\text{in } \mathrm{D}-\Omega) \tag{30}$$

$$\boldsymbol{\sigma}(\mathbf{x})=\boldsymbol{\sigma}_0^{\infty}+\mathbf{C}_0:\bar{\mathbf{G}}(\mathbf{x}):\boldsymbol{\varepsilon}_0^{**} \quad (\text{in } \mathrm{D}-\Omega) \tag{31}$$

with

$$\boldsymbol{\varepsilon}_0^{\infty}=-\frac{f_1}{1-f_1}\mathbf{C}_0^{-1}:\mathbf{P}^0, \quad \boldsymbol{\sigma}_0^{\infty}=-\frac{f_1}{1-f_1}\mathbf{P}^0, \quad \boldsymbol{\varepsilon}_0^{**}=(\mathbf{S}+\mathbf{M})^{-1}:\left(\mathbf{N}:\boldsymbol{\varepsilon}^{p_0}+\frac{f_1}{1-f_1}\mathbf{C}_0^{-1}:\mathbf{P}^0\right) \tag{32}$$

5 Benchmark of the micromechanics model

Although the Exterior-Point Eshelby tensor is introduced in the present micromechanics model, the derivations of the local elastic fields of closed-cell porous media with initial pressure are relatively complicated. Therefore, it is necessary to verify the reliability and accuracy of the present model. Here we consider an elastic spherical shell with closed fluid, as shown in Fig. 5. The inner radius of the sphere is denoted by *a*, and the outer radius by *b*. The inside hollow ball is filled by static fluid with initial pressure p_0. The uniform pressure $\bar{p}$ is applied on the outside surface of the spherical shell.

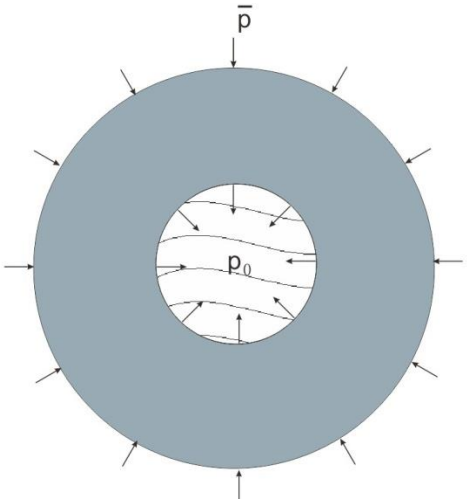

Figure 5: Elastic spherical shell subjected to internal pressure and external uniform load

For this simple problem, the classical approach in elasticity can be used to formulate the exact solution. When the elastic spherical shell is only subjected to the initial internal pressure p_0, the boundary conditions are given by

$$\left(\sigma_R\right)_{R=a} = -p_0, \quad \left(\sigma_R\right)_{R=b} = 0 \tag{33}$$

The radial stress component σ_R and tangential component σ_T can be derived as

$$\sigma_R = -\frac{\frac{1}{R^3}-\frac{1}{b^3}}{\frac{1}{a^3}-\frac{1}{b^3}}\,p_0, \quad \sigma_T = \frac{\frac{1}{2R^3}+\frac{1}{b^3}}{\frac{1}{a^3}-\frac{1}{b^3}}\,p_0 \tag{34}$$

where R is the radius of an arbitrary point in solid matrix.

We continue to consider the spherical shell only subjected to external uniform pressure $\bar{p}$, the corresponding boundary conditions are

$$\left(\sigma_R\right)_{R=a} = -p_0', \quad \left(\sigma_R\right)_{R=b} = -\bar{p} \tag{35}$$

where p_0' is the internal pressure of the fluid caused by the external uniform pressure $\bar{p}$. The corresponding solutions of the radial stress $\bar{\sigma}_R$ and the tangential stress $\bar{\sigma}_T$ are given by

$$\bar{\sigma}_R = -\frac{\frac{b^3}{R^3}-1}{\frac{b^3}{a^3}-1}\,p_0' - \frac{1-\frac{a^3}{R^3}}{1-\frac{a^3}{b^3}}\,\bar{p}, \quad \bar{\sigma}_T = \frac{\frac{b^3}{2R^3}+1}{\frac{b^3}{a^3}-1}\,p_0' - \frac{1+\frac{a^3}{2R^3}}{1-\frac{a^3}{b^3}}\,\bar{p} \tag{36}$$

According to the superposition principle, under both initial inner pressure and external uniform pressure, the total stress field σ_R^t of the elastic shell structure can be expressed by

$$\sigma_R^t = \sigma_R + \bar{\sigma}_R, \quad \sigma_T^t = \sigma_T + \bar{\sigma}_T \tag{37}$$

In order to verify the accuracy of the formulae of the local elastic fields of the special elastic shell, the comparisons between the exact solution and the present micromechanics-based solution are made in what follows. Material parameters and geometric dimensions used in this example benchmark are shown in Tab. 1.

Table 1: Material and geometric parameters of the spherical elastic shell

E_0 (MPa)	v_0	K_1 (MPa)	p_0 (MPa)	$\bar{p}$ (MPa)	a (mm)	b (mm)
6000	0.25	2250	10	20	100	150

The comparisons of radial stress σ_R and tangential stress σ_T calculated by the two approaches are given in Fig. 6 and Fig. 7. It is shown that the radial stress σ_R increases with the increase of the radius, while the tangential stress σ_T decreases with the increase of the radius. It is noted that the present micromechanics-based solutions are identical to the exact solutions, which demonstrates that the formulae of the local elastic fields derived by the micromechanical model are accurate and reliable. Furthermore, the results show that, even in a large volume fraction of fluid inclusions, the present micromechanics-based model still keeps high accuracy.

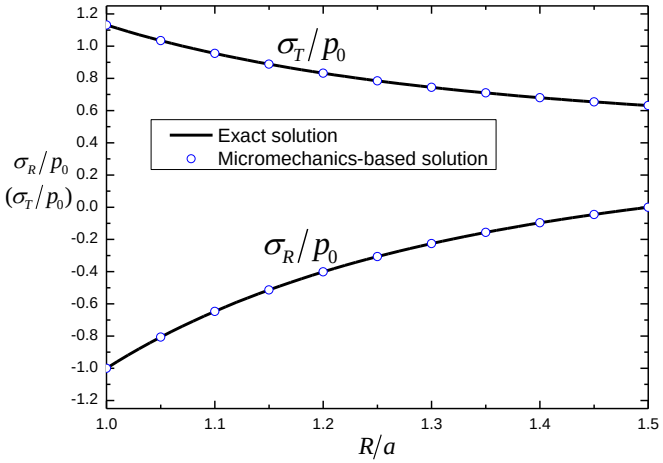

Figure 6: Comparison between exact solution and micromechanics-based solution for radial and tangential stresses of the elastic shell subjected to an internal pressure

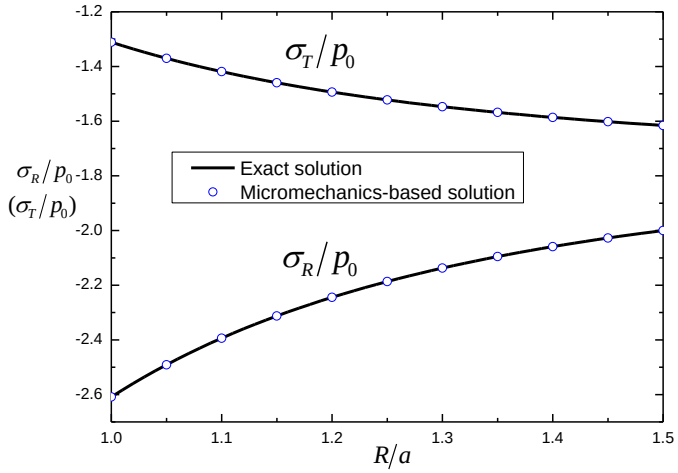

Figure 7: Comparison between exact solution and micromechanics-based solution for radial and tangential stresses of the elastic shell subjected to both internal pressure and external load

6 Application to porous media with spheroidal pores

For the closed-cell porous media containing the initial fluid pressure, it is difficult to derive the local elastic fields by the classical elastic mechanics approach, due to the complexity of the pore shape. As an application of the present micromechanics-based model, two numerical examples for the elastic fields of closed-cell porous materials with spheroidal pores are given.

We first consider the local elastic fields of the RVE of a porous medium with by a fluid-filled crack. As a classical example, Pollard et al. [Pollard and Segall, 1987] investigated the local elastic fields for two-dimensional crack in the elastic matrix. For the investigated three-dimensional fluid-filled prolate crack, the length of the semi-major axis, a_0, is assumed to be considerably larger than those of semi-minor axes, b_0, with an aspect ratio of $a_0/b_0 = 20$. For illustration purposes, the RVE of a porous medium with an isolated crack is shown in Fig. 8.

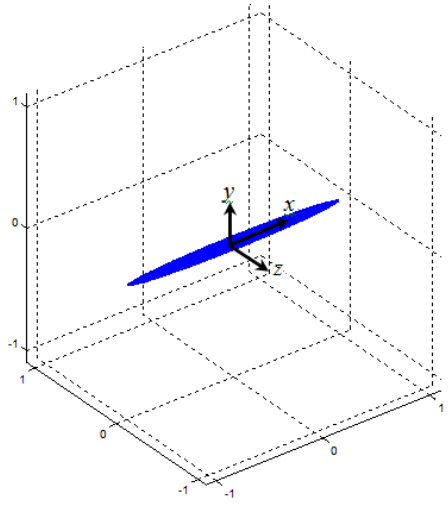

Figure 8: The RVE of a porous medium with an isolated crack

The adopted material parameters are the same as the previous example in Section. 5. The initial fluid pressure of the crack is set to $p_0 = 5$ MPa. Fig. 9 shows a contour plot of the normalized stress σ_{xx}/p_0 along the x direction in the $x-y$ plane of the RVE under the initial fluid pressure. The elastic stress field is symmetric and the maximum stress occurs in the crack tip due to stress concentration. We continue to apply uniformly distributed pressure $\overline{p_0} = 2$ MPa on the boundary of the RVE along the x direction. The contours of the normalized stress σ_{xx}/p_0 along the x direction in the $x-y$ plane of the RVE are plotted in Fig. 10. The compression of the fluid in the closed crack leads to an increase of the fluid pressure, which illustrates that the magnitudes of the normalized stresses σ_{xx}/p_0 at crack tips increase significantly.

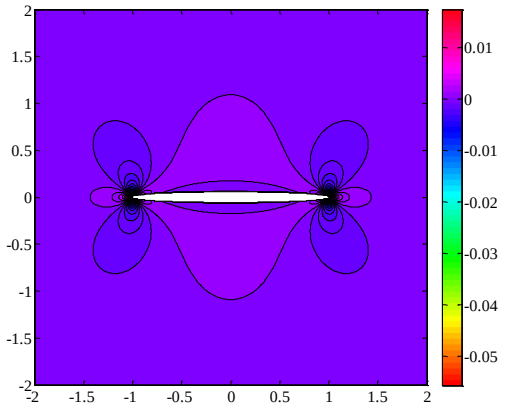

Figure 9: Contour map of the normalized stress σ_{xx}/p_0 around isolated crack in $x-y$ plane of the RVE due to an initial fluid pressure

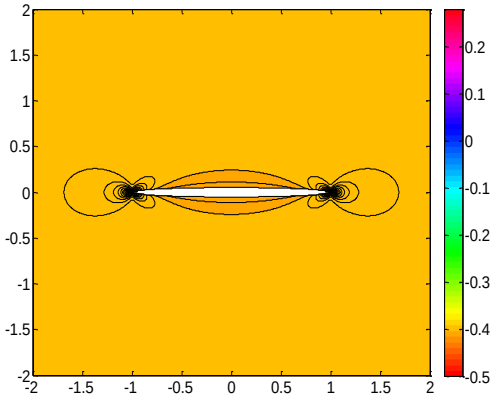

Figure 10: Contour map of the normalized stress σ_{xx}/p_0 around isolated crack in $x-y$ plane of the RVE due to an applied external pressure along *x* direction

For the RVE of a porous medium subjected to the initial fluid pressure and uniaxial distributed pressure at boundary, the 3D views of isosurfaces of the normalized stresses ($\sigma_{xx}/p_0 = -0.4, 0$) in matrix are shown in Fig. 11 and Fig. 12, respectively. The regions of the normalized stresses around the crack form symmetric and toroidal zones enclosing the crack.

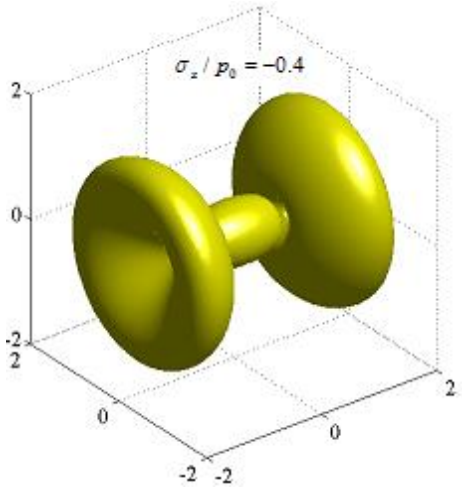

Figure 11: Isosurfaces of the normalized stress $\sigma_{xx}/p_0 = -0.4$ in matrix produced by the initial fluid pressure and uniaxial distributed pressure at boundary

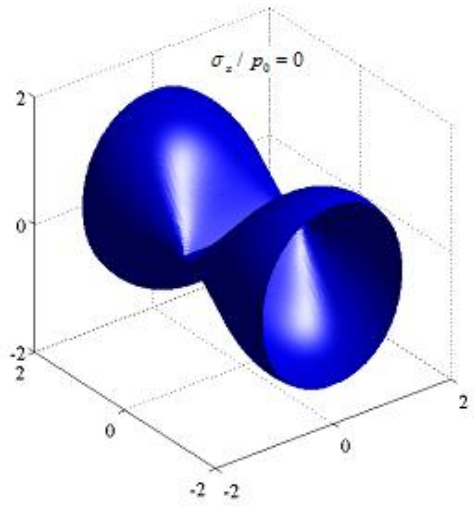

Figure 12: Isosurfaces of the normalized stress $\sigma_{xx}/p_0 = 0$ in matrix produced by the initial fluid pressure and uniaxial distributed pressure at boundary

Next, we consider the second illustrative example for the elastic fields of the porous media with the generally spheroidal fluid-filled pores. For the spheroidal pores, the lengths of semi-major axis and the semi-minor axis are set to $a_0 = 1.5$ mm, $b_0 = c_0 = 1\text{mm}$, respectively. The reference frame of the RVE used in this example is depicted in Fig. 13. The initial fluid pressure of the pore is set to $p_0 = 3\text{MPa}$. When a uniformly distributed pressure $\overline{p} = 5\text{MPa}$ is imposed on the boundary of the RVE along the *x* direction, the fluid pressure in spheroidal pore is increased to $3.9\,\text{MPa}$. Under this situation, the contour plots of the normalized stresses (σ_{xx}/p_0, σ_{yy}/p_0 and σ_{zz}/p_0) in matrix along three directions in the *x-y* plane are shown in Fig. 14. It is readily observed that the contour maps are symmetric about the central axes of the pore. With the combination of initial fluid pressure and applied external compressive loads, the components of the normalized stresses are quite different.

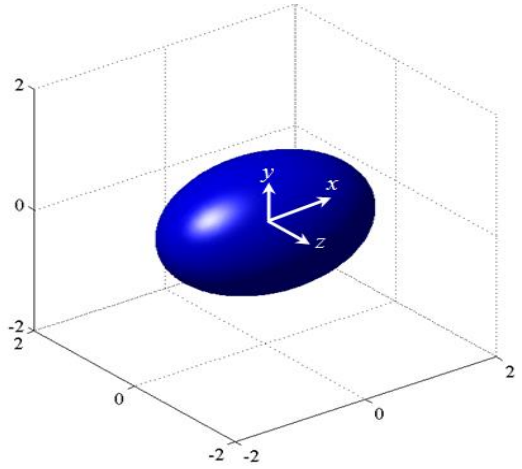

Figure 13: The RVE with a fluid-filled spheroidal pore

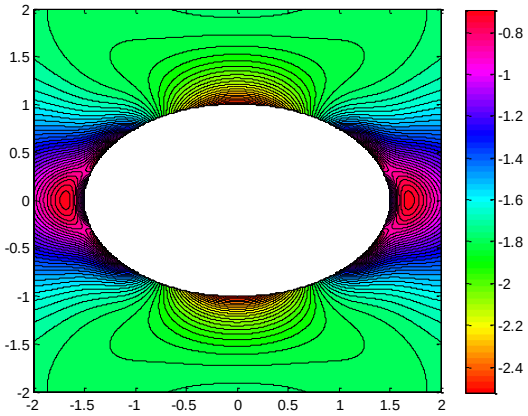

(a) σ_{xx}/p_0

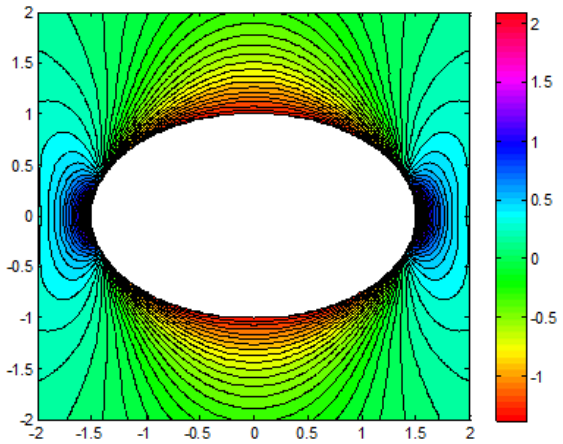

(b) σ_{yy}/p_0

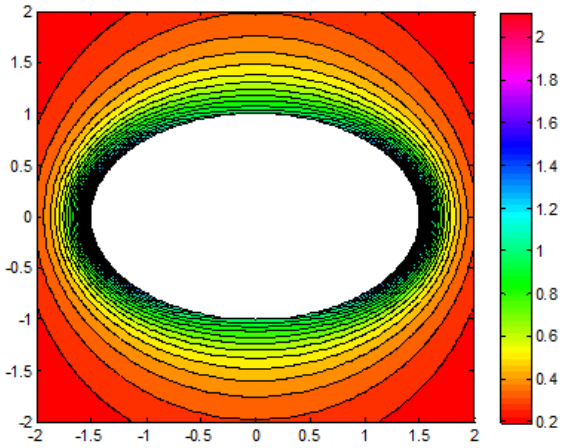

(c) σ_{zz}/p_0

Figure 14: Contour maps of the normalized stresses σ_{xx}/p_0 , σ_{yy}/p_0 and σ_{zz}/p_0 around the spheroidal pore in $x-y$ plane

For the 3D view, Fig. 15 shows the isosurfaces of the normalized stress σ_{xx}/p_0 around the spheroidal pore. The isosurfaces of $\sigma_{xx}/p_0=-1$, $\sigma_{xx}/p_0=-5/3$ and $\sigma_{xx}/p_0=-2$ are marked with yellow, red and blue color, respectively. The compressive shadows alongside the pore are radially symmetric about the central axes of pore.

When a uniform shear stress $\bar{\sigma}_{xy}=3\text{MPa}$ is applied on the boundary of the RVE of the porous medium, the fluid pressure in the pore remains unchanged, due to the inability of

the closed fluid to transfer the shear stress. The isosurfaces of the normalized maximum shear stresses ($\sigma_{xy}^{\max} / p_0 = 1.15$, $\sigma_{xy}^{\max} / p_0 = 1.10$ and $\sigma_{xy}^{\max} / p_0 = 1.05$) in matrix around the pore, are shown in yellow, red and blue color, respectively (see Fig. 16). Regions of the normalized shear stress around the spheroidal pore are also radially symmetric about the central axes of pore.

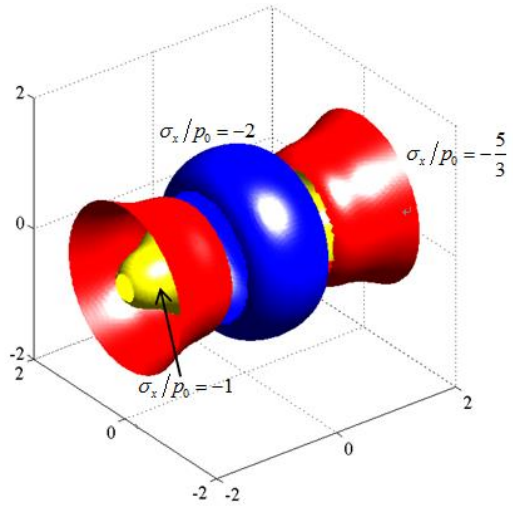

Figure 15: Isosurfaces of the normalized stress σ_{xx} / p_0 in matrix due to the initial fluid pressure and uniaxial compressive load

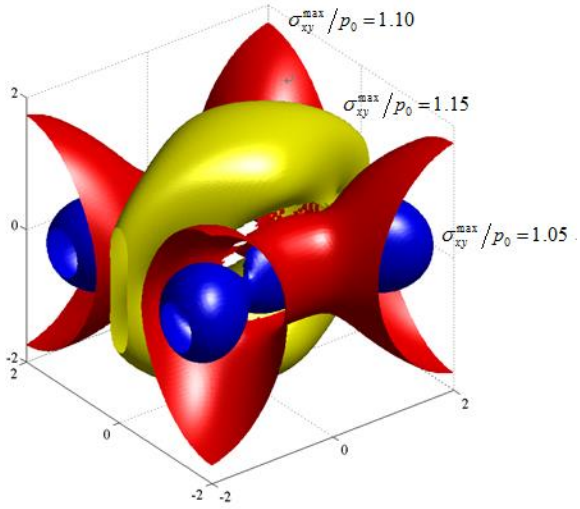

Figure 16: Isosurfaces of the normalized stress $\sigma_{xy}^{\max} / p_0$ in matrix due to the initial fluid pressure and uniaxial compressive load

7 Conclusions

In this paper, a micromechanics-based model is developed to determine the local elastic fields of the closed-cell porous media with initially pressurized spheroidal pores. In this model, the equivalent far-field method is used to transform the problem of finite volume fraction of pores into that of infinite matrix, and the initial fluid pressure is represented by introducing an initial eigenstrain in the fluid-filled pore by equivalent inclusion method. With a benchmark example of an elastic spherical shell structure, the reliability and accuracy of the present micromechanics model are validated, even in the case of finite volume fraction of fluid-filled pores. For the porous media with initially pressurized spheroidal pores subjected to uniform external loads, several numerical examples for the local elastic fields around the fluid-filled prolate crack-like pore and generally spheroidal pore are respectively illustrated. It is noted that the present micromechanics model, for the determination of elastic fields, can also be extended to the porous media with multiple and randomly distributed fluid-filled pores.

Acknowledgement: The supports from the National Natural Science Foundation of China (Grant No. 11572109), the Hebei Natural Science Foundation of China (Grant No. A2016201198), the Key project of science and technology research in Colleges and Universities of Hebei Province (Grant No. ZD2017006) and the China Scholarship Council are gratefully acknowledged.

References

Biot, M. A. (1954): Theory of elasticity and consolidation for a porous anisotropic solid. *Journal of Applied Physics*, vol. 26, no. 2, pp. 182-191.

Chen, J. K; Zhu, J.; Wang, J.; Yuan, M.; Chu, H. J. (2006): The properties of the Poisson's ratio of microcellular foams with low porosity: non-stationary, negative value, and singularity. *Mechanics of Time-Dependent Materials*, vol. 10, pp. 315-330.

Duan, H. L.; Wang, J.; Huang, Z. P.; Zhong, Y. (2005): Stress fields of a spheroidal inhomogeneity with an interphase in an infinite medium under remote loadings. *Proceedings of the Royal Society A: Mathematical, Physical and Engineering Sciences*, vol. 461, no. 2056, pp. 1055-1080.

Eshelby, J. D. (1957): The determination of the elastic field of an ellipsoidal inclusion, and related problems. *Proceedings of the Royal Society of London. Series A, Mathematical and Physical Sciences*, vol. 241, no. 1226, pp. 376-396.

Gassmann, F. (1951): On elasticity of porous media. *Vierteljahrsschrift der Naturforschenden Gesellschaft in Zürich*, vol. 96, pp. 1-23.

Gologanu, M.; Leblond, J. B.; Devaux, J. (1994): Approximate models for ductile metals containing nonspherical voids-case of axisymmetric oblate ellipsoidal cavities. *Journal of Engineering Materials and Technology*, vol. 116, no. 3, pp. 290-297.

Guo, Q.; Liu, X.; Hu, G. (2006): Micromechanical modeling of local field distribution for a planar composite under plastic deformation. *Acta Mechanica*, vol. 187, pp. 139-149.

Guo, T. F.; Cheng, L. (2002): Modeling vapor pressure effects on void rupture and crack growth resistance. *Acta Materialia, vol.* 50, no. 13, pp. 3487-3500.

Gurson, A. L. (1977): Continuum theory of ductile rupture by void nucleation and growth: Part I-Yield criteria and flow rules for porous ductile media. *Journal of Engineering Materials and Technology,* vol. 99, no. 1, pp. 2-15.

Hartmann, C.; Delgado, A. (2004): Numerical simulation of the mechanics of a yeast cell under high hydrostatic pressure. *Journal of biomechanics,* vol. 37, no. 7, pp. 977-987.

Hartmann, C.; Mathmann, K.; Delgado, A. (2006): Mechanical stresses in cellular structures under high hydrostatic pressure. *Innovative Food Science & Emerging Technologies,* vol. 7, no. 1-2, pp. 1-12.

Hu, G. K.; Weng, G. J. (1998): Influence of thermal residual stresses on the composite macroscopic behavior. *Mechanics of Materials,* vol. 27, no. 4, pp. 229-240.

Huang Q. Z.; Zheng, X. P.; Yao, Z. H. (2011): Boundary element method for 2D solids with fluid-filled pores. *Engineering Analysis with Boundary Elements,* vol. 35, no. 2, pp. 191-199.

Ju, J. W.; Sun, L. Z. (1999): A novel formulation for exterior-point Eshelby's tensor of an ellipsoidal inclusion. *Journal of Applied Mechanics,* vol. 66, pp. 570-574.

Julien, J.; Gărăjeu, M.; Michel, J. C. (2011): A semi-analytical model for the behavior of saturated viscoplastic materials containing two populations of voids of different sizes. *International Journal of Solids and Structures,* vol. 48, no. 10, pp. 1485-1498.

Kachanov, M.; Tsukrov, I.; Shafiro, B. (1995): Materials with fluid-saturated cracks and cavities: fluid pressure polarization and effective elastic response. *International Journal of Fracture,* vol. 73, no. 4, pp. 61-66.

Kitazono, K.; Sato, E.; Kuribayashi, K. (2003): Application of mean-field approximation to elastic-plastic behavior for closed-cell metal foams. *Acta Materialia,* vol. 51, no. 16, pp. 4823-4836.

Ma, L. H.; Rolfe, B. F.; Yang, Q. S.; Yang, C. H. (2011): The configuration evolution and macroscopic elasticity of fluid-filled closed-cell composites: micromechanics and multiscale homogenization modelling. *Computer Modeling in Engineering & Sciences,* vol. 79, no. 2, pp. 131-158.

Ma, L. H.; Yang, Q. S.; Yan, X. H.; Qin, Q. H. (2014): Elastoplastic mechanics of porous media with varied inner pressures. *Mechanics of Materials,* vol. 73, pp. 58-75.

Mikata, Y.; Taya, M. (1985): Stress field in and around a coated short fiber in an infinite matrix subjected to uniaxial and biaxial loadings. *Journal of Applied Mechanics,* vol. 52, no. 1, pp. 19-24.

Mura, T. (1987): *Micromechanics of Defects in Solids.* Martinus Nijhoff Publishers.

O'Connell, R. J.; Budiansky, B. (1977): Viscoelastic properties of fluid-saturated cracked solid. *Journal of Geophysical Research,* vol. 82, no. 36, pp. 5719-5735.

Ozgur, M.; Mullen, R. L.; Welsch, G. (1996): Analysis of closed cell metal composites. *Acta Materialia,* vol. 44, no. 5, pp. 2115-2126.

Pollard, D. D.; Segall, P. (1987): Theoretical displacements and stresses near fractures in rock: with applications to faults, joints, veins, dikes, and solution surfaces. *Fracture Mechanics of Rock*, Academic Press, London, pp. 277-349.

Ponte Castañeda, P. (1991): The effective mechanical properties of nonlinear isotropic composites. *Journal of the Mechanics and Physics of Solids*, vol. 39, no. 1, pp. 45-71.

Shafiro, B.; Kachanov, M. (1997): Materials with fluid-filled pores of various shapes: effective elastic properties and fluid pressure polarization. *International Journal of Solids and Structures*, vol. 34, no. 27, pp. 3517-3540.

Takao, Y.; Taya, M. (1985): Thermal expansion coefficients and thermal stresses in an aligned short fiber composite with application to a short carbon fiber/aluminum. *ASME Journal of Applied Mechanics*, vol. 52, no. 4, pp. 806-810.

Terzaghi, K. (1943): *Theoretical soil mechanics*. John Wiley & Sons, Inc.

Thomsen, L. (1995): Elastic anisotropy due to aligned cracks in porous rocks. *Geophysical Prospecting*, vol. 43, no. 6, pp. 805-829.

Vincent, P. G.; Monerie, Y.; Suquet, P. (2009): Porous media with two populations of voids under internal pressure: I. Instantaneous constitutive relations. *International Journal of Solids and Structures*, vol. 46, no. 3-4, pp. 480-506.

Yang, Q. S.; Becker, W. (2004): A comparative investigation of different homogenization methods for prediction of the macroscopic properties of composites. *Computer Modeling in Engineering & Sciences*, vol. 6, no. 4, pp. 319-332.

Yang, Q. S.; Li, C. J. (2006): Evolution of properties in hydration of cements-a numerical study. *Mechanics Research Communications*, vol. 33, no. 5, pp. 717-727.

Yang, Q. S.; Tao, X.; Yang, H. (2007): A stepping scheme for predicting effective properties of the multi-inclusion composites. *International Journal of Engineering Science*, vol. 45, no. 12, pp. 997-1006.

Zhang, H. W.; Lv, J.; Zheng, Y. G. (2010): A new multiscale computational method for mechanical analysis of closed liquid cell materials. *Computer Modeling in Engineering & Sciences*, vol. 68, no.1, pp. 55-93.

Zhang, W. X.; Xu, Z. M.; Wang, T. J.; Chen, X. (2009): Effect of inner gas pressure on the elastoplastic behavior of porous media: A second-order moment micromechanics model. *International Journal of Plasticity*, vol. 25, no. 7, pp. 1231-1252.